MATERIALS PHYSICS AND MECHANICS RESEARCH ARTICLE

Submitted: February 4, 2026 **Revised: March 10, 2026** **Accepted: March 16, 2026**

Partitioning of a microstructure produced during laser powder bed fusion of 17-4 PH steel

S.I. Borisov [1], P.D. Dolzhenko [1], I.S. Nikitin [1], A.A. Kalinenko [1], I.S. Zuiko [1], E.V. Kaliuzhnaya [1], L. Shi [2], Ch. Wu[2], S.Yu. Mironov [1]✉

[1] Belgorod National Research University, Belgorod, Russia

[2] Shandong University, Jinan, China

✉ mironov@bsuedu.ru

ABSTRACT

This study focused on the characterization of a complex microstructure in 17-4 PH martensitic steel produced during laser powder bed fusion. Due to the specific nature of the LPBF process, the additive material undergoes an extremely high cooling rate (~ 10^6 K/s) and pronounced thermal cycling. This usually gives rise to the complex microstructures consisting of δ-ferrite, austenite, and martensite. In this work, a two-step approach was developed for the partitioning of the δ-ferrite and martensite phases. The elaborated method was based on the electron backscatter diffraction technique and involved a two-factor filtration of the electron backscatter diffraction data using the distinct differences between the δ-ferrite and martensite in stored energy and grain size. From experimental observations, it was shown that the proposed technique was highly effective for an analysis of the complex microstructures produced during LPBF of 17-4 PH martensitic steel.

KEYWORDS

martensitic steel • additive manufacturing • electron backscatter diffraction • microstructure • martensite δ-ferrite

Funding. *The work was supported by the government assignment FZWG-2026-0005 "Development of scientific foundations for optimization of selective laser melting and subsequent heat treatment of precipitation-hardening martensitic steel 17-4 PH", Ministry of Science and Higher Education of the Russian Federation. The experimental works were conducted using equipment of the Joint Research Center "Technology and Materials" at Belgorod State National Research University.*

Citation: Borisov SI, Dolzhenko PD, Nikitin IS, Kalinenko AA, Zuiko IS, Kaliuzhnaya EV, Shi L, Wu Ch, Mironov SYu. Partitioning of a microstructure produced during laser powder bed fusion of 17-4 PH steel. *Materials Physics and Mechanics*. 2026;54(2): 17–25.
http://dx.doi.org/10.18149/MPM.5422026_2

Introduction

Owing to a good balance of strength and corrosion resistance, 17-4 PH martensitic steel is widely used in aerospace, petrochemical, and marine industries. Moreover, a recent invention of the additive laser powder bed fusion (LPBF) technology may further broaden the application range of this material for the fabrication of complex-shaped parts.

The LPBF technology involves the incremental, layer-by-layer melting and fusion of an atomized metal powder by a laser beam following an appropriate computer model [1,2]. Due to the specific nature of the LPBF process, the manufactured material experiences a non-trivial thermal history involving an extremely high cooling rate (~10^6 K/s) and a pronounced thermal cycling, including several melting-to-solidification sequences. In the 17-4 PH steel, LPBF often gives rise to the complex microstructures consisting of

an intermixture of δ-ferrite, austenite, and martensite [3–20]. To ascertain the key microstructural mechanisms involved in the LPBF process as well as to predict the service properties of LPBFed parts, a quantification of these phases is necessary. However, while a detection of the austenitic phase is rather straightforward, the differentiation between the δ-ferrite and martensite is challenging because of the similarity of the crystal structure of the phases.

To surmount this issue, several approaches based on the electron backscatter diffraction (EBSD) technique have been proposed in the scientific literature [15,16,21–30]. Typically, those are based on the presumed distinction of the stored energy between the ferrite and martensite and the concomitant difference in the lattice imperfections. Hence, the distribution of a related EBSD metric (which is sometimes referred to as the image quality index[1]) should be either bimodal or exhibit a clear transition from one phase to another.

From the authors' experience, however, the experimental distributions of image quality (IQ) index are often smooth and show no clear transition between the phases. Therefore, the resulting microstructure partitioning is not always perfect.

To enhance the efficiency of this procedure, a two-step approach was suggested in the present study. In this case, the conventional IQ-based partitioning technique is complemented by an additional filtration step, which is based on another distinct characteristic of the martensitic phase. The latter one may include a relatively low confidence index of diffraction patterns, a broader grain orientation spread, or a finer grain size. It was assumed that such a two-factor data filtration strategy would increase the efficiency of phase partitioning. This work was undertaken to investigate the validity of this concept.

Materials and Methods

The program material used in this work was a commercial 17-4 PH martensitic steel with the nominal chemical composition shown in Table 1. The material was produced by 3D Systems Inc. using the nitrogen-gas atomization technique and supplied as an atomized metallic powder. The powder particles had a nearly spherical morphology and often contained satellites. The particle size distribution was relatively broad, spanning from ~ 1 to ≈ 30 μm.

Table 1. Nominal chemical composition of 17-4 PH martensitic steel (wt. %)

Fe	Cr	Ni	Cu	Mn	Si	Ta + Nb	C	P	S
Balance	15.0–17.5	3.0–5.0	3.0–5.0	⩽ 1.0	⩽ 1.0	0.15–0.45	⩽ 0.07	⩽ 0.04	⩽ 0.03

The LPBF process was carried out on a ProX DMD 200 machine (3D Systems). To minimize porosity, LPBF variables were selected to provide a relatively high volumetric energy density. Those included a laser power of 180 W, a laser scanning speed of 1 m/s, a hatch distance of 50 μm, and a powder layer thickness of 30 μm (the volumetric energy density of 120 J/mm^3). A cuboidal-shaped sample with dimensions 10 × 10 × 20 mm^3 was built vertically using a nitrogen atmosphere. A simple parallel scan strategy was employed

[1]In TSL OIM software, the image quality (IQ) index characterizes the sharpness of the Kikuchi bands in a digitized diffraction pattern and thus serves as a qualitative measure of stored energy.

with a 90° rotation of the laser scan direction from layer to layer. No heat treatment was applied after the LPBF procedure.

For EBSD observations, the built sample was sectioned in half along the building direction, mounted into a conductive KonductoMet resin, and mechanically polished using standard metallographic procedures. A final surface finish was achieved using 24-h vibratory polishing with OP-S colloidal silica suspension.

EBSD analysis was performed employing an FEI Quanta 600 field-emission-gun scanning electron microscope (FEG-SEM) equipped with TSL OIM™ software and operated at an accelerated voltage of 20 kV. Microstructural observations were focused on the central part of the built sample. To provide both a necessary spatial resolution and sufficient sampling statistics, an intermediate EBSD scan step size of 0.2 μm was applied. Given the above-mentioned difficulty of discriminating ferrite from martensite in EBSD, these two phases were indexed as the generic body-centered cubic (BCC) phase; accordingly, the austenite was indexed as the generic face-centered cubic (FCC) phase. To enhance the reliability of EBSD data, the fine grains comprising two or one pixel were automatically "cleaned" from the acquired EBSD map using the standard grain-dilation option of EBSD software.

Results and Discussion

Preliminary analysis

The EBSD IQ map of a typical microstructure evolved in the central part of the built sample[2] is shown in Fig. 1(a). In the map, the FCC phase is highlighted with red, while the BCC component is shown in gray.

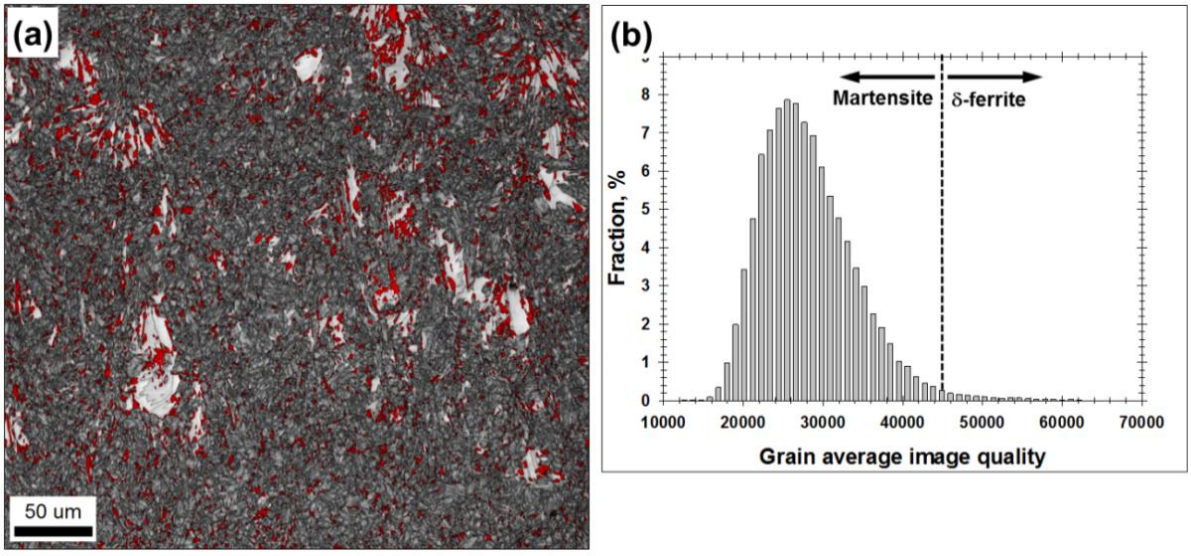

Fig. 1. (a) EBSD image-quality map of evolved microstructure (austenitic phase is highlighted with red) and (b) the distribution of the grain average image-quality index derived from the BCC microstructural component and used for the separation of martensite and d-ferrite. In (b), a presumed transition from martensite to d-ferrite is shown

[2]The volume fraction of the retained porosity within the LPBD'ed sample was measured to be ≈ 0.2 %.

The FCC constituent was obviously austenite. Remarkably, the austenite volume fraction was measured at ≈ 12.6 %, thus being comparatively high for 17-4 PH martensitic steel. Moreover, given the fine-scale nature of the produced microstructure (Fig. 1(a)), it is likely that some fraction of the austenite particles was "missed" during EBSD mapping, and thus the real proportion of this phase was even higher. The increased austenite content was likely attributable to both the relatively high cooling rate during LPBF and the influence of the nitrogen atmosphere.

In the context of the present study, of particular interest was the BCC microstructure. To a first approximation, it consisted of two distinct components, viz., coarse-grained and fine-grained ones.

The coarse-grained BCC component often exhibited columnar grain morphology and a comparatively bright IQ contrast (i.e., the low stored energy). Hence, this microstructural constituent was likely δ-ferrite. The preservation of the metastable δ-ferrite in the microstructure suggested the extremely high cooling rate during the LPBF. Remarkably, the δ-ferrite grains were not distributed uniformly throughout the microstructure but tended to cluster in local areas. Those presumably represented the remnants of the local molten pools, which are characteristic of the LPBF process.

Contrarily, the fine-grained BCC component showed a lath-shaped morphology and a comparatively dark IQ contrast (i.e., the high stored energy). From a broad perspective, therefore, this microstructural constituent reflected martensite. Noteworthy, the martensite was the dominant phase in the produced material, as is normally expected for the 17-4 PH martensitic steel.

Thus, in agreement with the scientific literature [3–20], the produced microstructure represented a complex mixture of δ-ferrite, austenite, and martensite. While the austenitic phase was readily recognizable, the unbiased distinguishing of δ-ferrite and martensite was challenging.

Microstructure partitioning. Step 1

To discriminate the δ-ferrite and martensite phases, the conventional IQ-based technique was first applied. The distribution of the grain average IQ indexes derived from the BCC microstructural constituent is presented in Fig. 1(b). The distribution was not bimodal but exhibited a distinct asymmetry. Specifically, it consisted of a pronounced peak at a comparatively low IQ index and an extreme end ("tail") in the high IQ range. It was highly likely that the former characteristic represented martensite, while the latter one reflected δ-ferrite. However, the transition between the phases was smooth, and no clear threshold could be found. The broadly similar IQ distributions for ferrite-martensite microstructures have been reported in a number of works, e.g. [21–24].

Using a trial-and-error approach, the approximate threshold was defined at IQ = 45,000. For clarity, this presumed borderline between the phases was indicated by a dotted line in Fig. 1(b). Based on this threshold, the IQ map[3] for the BCC crystals (Fig. 2(a)) was partitioned into two microstructural components, as shown in Fig. 2(b,c). It was found that the grains with relatively low IQ index (IQ < 45,000) exhibited lamellar

[3]The grayscale IQ maps are often similar to the corresponding optical (or SEM) images of a microstructure. Accordingly, those can be simple for comparison with conventional metallography.

morphology and comparatively fine sizes (Fig. 2(b)). On the other hand, the data with a higher IQ index (IQ ⩾ 45,000) encompassed all coarse columnar-shaped grains but also included a fraction of fine-scale grains (Fig. 2(c)).

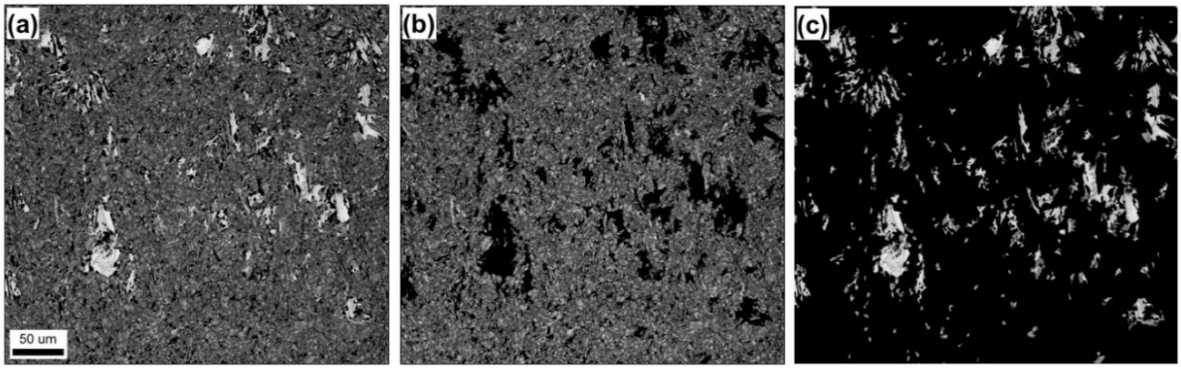

Fig. 2. EBSD image-quality maps showing microstructure partitioning of bcc phases (first step): (a) initial map, (b) "low-IQ" constituent, and (c) "high-IQ" constituent

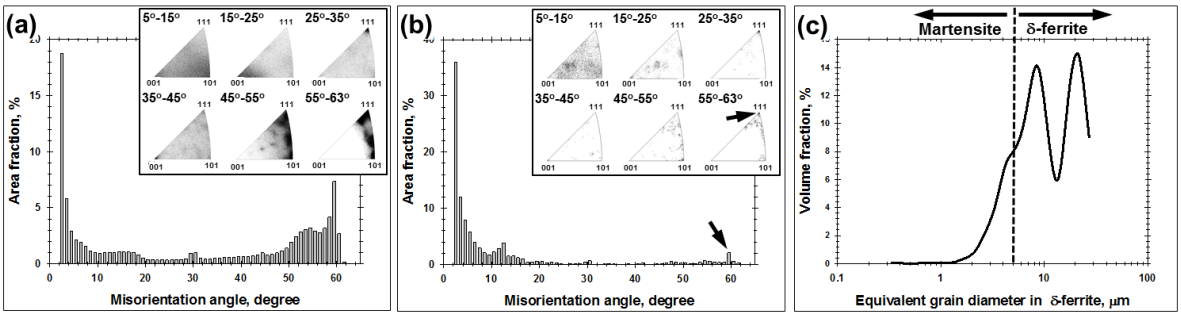

Fig. 3. Misorientation distributions derived from the partitioned phases (first step): (a) "low-IQ" microstructural constituent, (b) "high-IQ" microstructural constituent, and (c) grain-size distribution of the "high-IQ" microstructural constituent. In (a) and (b), misorientation-axis distributions are shown as inserts in the top right corners. In (b), arrows show an increased fraction of nearly-60° <111> boundaries, which presumably belonged to martensitic phase. In (c), a presumed transition from martensite to δ-ferrite is shown

To get additional insight into the partitioning results, misorientation distributions for both microstructural constituents were measured, as shown in Fig. 3(a,b). Due to the limited angular accuracy of EBSD, the lower-limit misorientation cut-off of 2° was applied in all cases.

The "low IQ" constituent showed a bimodal misorientation-angle distribution with a pronounced low-angle maximum and a broad peak in the range of 50–60° (Fig. 3(a)). Importantly, the misorientation axes of low-angle boundaries (LABs) tended to cluster near <101>, while those of the 50–60° boundaries preferentially concentrated near <111> and <101> (insert in the top right corner of Fig. 3(a)). The broadly similar misorientation distributions are normally observed in martensitic structures, e.g. [31–37] and are usually attributable to the dominance of the boundaries between martensite variants. Therefore, almost certainly, the "low IQ" microstructural constituent represented martensite.

The misorientation-angle distribution of the "high-IQ" microstructural constituent was dominated by low-angle boundaries but also included a subtle fraction of nearly 60° <111> boundaries (Fig. 3(b)). While the increased LAB content could readily be

associated with the dendritic origin of δ-ferrite, e.g. [15], the 60° <111> misorientations are hard to attribute to this phase. Moreover, a closer inspection showed that those boundaries were typically located within the relatively fine grains with relatively dark IQ contrast (Fig. 2(c)). Hence, those likely belonged to martensite, and therefore the partitioned δ-ferrite was probably contaminated by some fraction of this phase.

Microstructure partitioning. Step 2

Therefore, in accordance with expectations, the IQ-based approach was not entirely efficient. One probable reason for this effect could be the high residual stresses, which were presumably produced within the δ-ferrite phase due to an extremely high cooling rate during the LPBF process. This should degrade Kikuchi patterns and thus reduce the IQ index.

Accordingly, the second partitioning step was applied. From a series of preliminary experiments, it was found that the partitioning techniques based on either confidence index or grain orientation spread were not effective. Therefore, the grain size approach was used hereafter as the second data filtration step. This method was grounded on the presumed distinction in grain size between the δ-ferrite dendrites and martensite laths. The grain size was measured using the equivalent-grain diameter approach, i.e., by measurements of the grain area in the EBSD map and calculating the circle-equivalent diameter [38]. A 5-degree criterion was applied to define grain boundaries.

The grain size distribution derived from the partitioned δ-ferrite structure was shown in Fig. 3(c)[4]. Considering the specific character of the distribution, the grains below 5 μm in size were assumed to belong to the martensitic phase. For clarity, this presumed borderline between the martensite and δ-ferrite was indicated by a dotted line in Fig. 3(c). Based on this threshold, the IQ map for the BCC crystals (Fig. 4(a)) was partitioned into two microstructural components, as shown in Fig. 4(b,c). The misorientation distributions for the partitioned components were given in Fig. 5.

The second filtration step provided no apparent changes in either morphology or misorientation distribution of the presumed martensitic phase (Figs. 4(b) and 5(a)). In δ-ferrite, in contrast, the finest grains were filtered out (compare Figs. 4(c) and 2(c)). This eliminated the 60° <111> peak in the misorientation distribution (compare Figs. 5(b) and 3(b)).

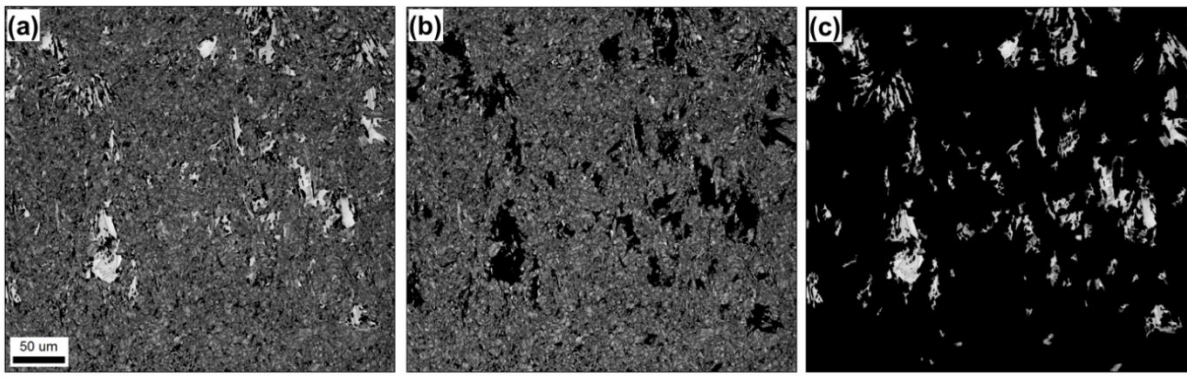

Fig. 4. EBSD image-quality maps showing microstructure partitioning of bcc phases (second step): (a) initial map, (b) partitioned martensite, and (c) partitioned δ-ferrite

[4]Given the scan step size of 0.2 μm applied during EBSD mapping, the finer grains (that may potentially exist in the microstructure) were not included in the grain-size distribution in Fig. 3(c).

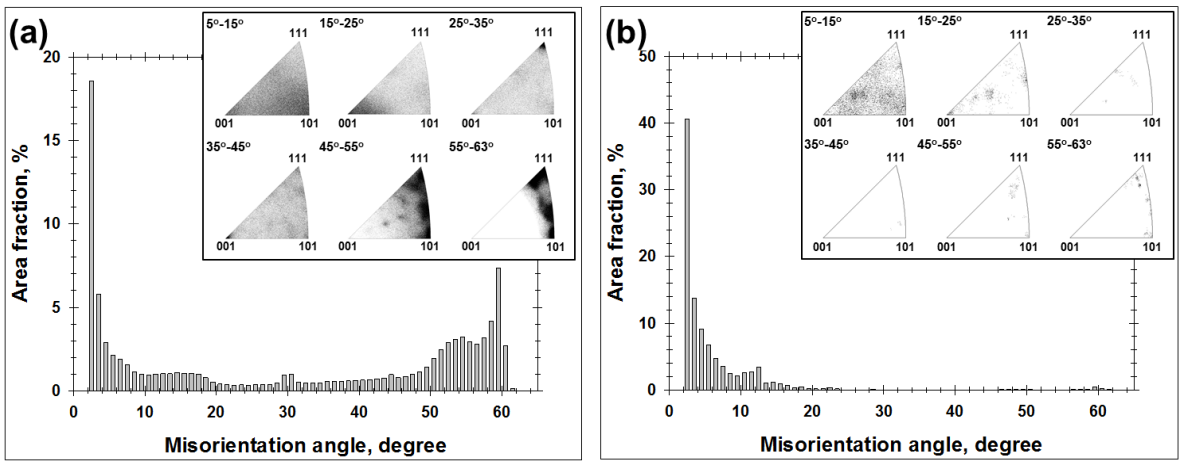

Fig. 5. Misorientation distributions derived from the partitioned phases (second step): (a) martensite and (b) δ-ferrite. In both cases, misorientation-axis distributions are shown as inserts in the top right corner

Premised on the latter observation, it was suggested that the δ-ferrite was filtered out from the martensite contaminations. Hence, it was concluded that the proposed two-step approach was effective for the partitioning of the δ-ferrite/martensite microstructure produced during LPBF of 17-4 PH martensitic steel.

It is worth noting that the conventional "one-step" IQ method is applicable to a wide range of ferrite-martensite structures [15,16,21–30]. It is likely, therefore, the relevance of the "two-step" technique developed in this study is not limited to the LPBF'ed 17-4 PH steel but also extends to a broader class of materials. On the other hand, the stress-relief annealing, which is often used for the LPBF'ed products, may reduce the difference in the stored energy between the martensite and δ-ferrite. This may obstruct the implementation of the approach.

Conclusions

This study was undertaken to provide an insight into the complex microstructure developed during LPBF of 17-4 PH steel. To this end, a two-step approach was proposed for the partitioning of the constituent δ-ferrite and martensite phases. This method was based on EBSD and involved a two-factor data filtration according to the distinct differences between the δ-ferrite and martensite in stored energy and grain size. The stored energy within the phases was evaluated employing a so-called image quality index, i.e., the EBSD metric characterizing the sharpness of the Kikuchi bands in digitized diffraction patterns. It was found the microstructure partitioning based on the stored energy only was not entirely effective. This observation was attributed to the high residual stresses, which were presumably produced within the δ-ferrite phase due to an extremely high cooling rate during the LPBF process. In contrast, the second-step partitioning on the basis of the grain size difference between the δ-ferrite and martensite was found to be effective for distinguishing these phases.

CRediT authorship contribution statement

Sergei I. Borisov: investigation, writing – review & editing; **Pavel D. Dolzhenko**: investigation, writing – review & editing; **Ivan S. Nikitin**: investigation, writing – review & editing; **Alexander A. Kalinenko**: investigation, writing – review & editing; **Ivan S. Zuiko**: investigation, writing – review & editing; **Elena V. Kaliuzhnaya**: writing – review & editing; **Lei Shi**: conceptualization, writing – review & editing; **Chuasong Wu**: conceptualization, writing – review & editing; **Sergei Yu. Mironov**: conceptualization, data curation, supervision, writing – original draft.

Conflict of interest

The authors declare that they have no conflict of interest.

References

1. Agarwala M, Bourell D, Beaman J, Marcus H, Barlow J. Direct selective laser sintering of metals. *Rapid Prototyping Journal.* 1999;1(1): 26–36.
2. Popovich AA, Sufiiarov VS, Borisov EV, Polozov IA, Masaylo DV. Design and manufacturing of tailored microstructure with selective laser melting. *Materials Physics and Mechanics.* 2018(1); 38: 1–10.
3. Murr LE, Gaytan SM, Ramirez DA, Martinez E, Hernandez J, Amato KN, Shindo PW, Medina FR, Wicker RB. Metal fabrication by additive manufacturing using laser and electron beam melting technologies. *Journal of Materials Science and Technology.* 2012;28(1): 1–14.
4. Akita M, Uematsu Y, Kakiuchi T, Nakajima M, Kawaguchi R. Defect-dominated fatigue behavior in type 630 stainless steel fabricated by selective laser melting. *Materials Science and Engineering: A.* 2016;666: 19–26.
5. Pasebani S, Ghayoor M, Badwe S, Irrinki H, Atre SV. Effects of atomizing media and post processing on mechanical properties of 17-4 PH stainless steel manufactured via selective laser melting. *Additive Manufacturing.* 2018;22: 127–137.
6. Vunnam S, Saboo A, Sudbrack C, Starr TL. Effect of powder chemical composition on the as-built microstructure of 17-4 PH stainless steel processed by selective laser melting. *Additive Manufacturing.* 2019;30: 100876.
7. Hsu TH, Chang YJ, Huang CY, Yen HW, Chen CP, Jen KK, Yeh AC. Microstructure and property of a selective laser melting process induced oxide dispersion strengthened 17-4 PH stainless steel. *Journal of Alloys and Compounds.* 2019;803: 30–41.
8. Wang X, Liu Y, Shi T, Wang Y. Strain rate dependence of mechanical property in a selective laser melted 17–4 PH stainless steel with different states. *Materials Science and Engineering: A.* 2020;792: 139776.
9. Sun Y, Hebert RJ, Aindow M. Effect of laser scan length on the microstructure of additively manufactured 17-4PH stainless steel thin-walled parts. *Additive Manufacturing.* 2020;35: 101302.
10. Yadollahi A, Mahmoudi M, Elwany A, Doude H, Bian L, Newman JC. Effects of crack orientation and heat treatment on fatigue-crack-growth behavior of AM 17-4 PH stainless steel. *Engineering Fracture Mechanics.* 2020;226: 106874.
11. Lee HJ, Dao VH, Ma YW, Yu JM, Yoon KB. Effects of process parameters on the high temperature strength of 17-4PH stainless steel produced by selective laser melting. *Journal of Mechanical Science and Technology.* 2020;34(8): 3261–3272.
12. Sabooni S, Chabok A, Feng SC, Blaauw H, Pijper TC, Yang HJ, Pei YT. Laser powder bed fusion of 17–4 PH stainless steel: A comparative study on the effect of heat treatment on the microstructure evolution and mechanical properties. *Additive Manufacturing.* 2021;46: 102176.
13. Ponnusamy P, Sharma B, Masood SH, Rahman Rashid RA, Rashid RR, Palanisamy S, Ruan D. A study of tensile behavior of SLM processed 17-4 PH stainless steel. *Materials Today: Proceedings.* 2021;45: 4531–4534.
14. Aripin MA, Sajuri Z, Syarif J, Baghdadi AH, Mohamed IF. Evaluation of microstructure and porosity for 3D printed stainless steel. *Materials Today: Proceedings.* 2022;66: 3082–3086.
15. Vysotskiy I, Malopheyev S, Zuiko I, Mironov S, Kaibyshev R. Crystallographic aspects of 17–4 PH martensitic steel produced by laser-powder bed fusion. *Materials Characterization.* 2022;194: 112405.
16. Vysotskiy I, Malopheyev S, Zuiko I, Mironov S, Kaibyshev R. Microstructure distribution in 17-4 PH martensitic steel produced by selective laser melting. *Metallurgical and Materials Transactions A.* 2022;53: 4143–4147.

17. Yasa E, Atik I, Kandemir I. Material-specific phenomena and developing higher yield process parameters in laser powder bed fusion of 17-4 PH stainless steel. *Journal of the Brazilian Society of Mechanical Sciences and Engineering.* 2023;45: 38.
18. Mazruee Sebdani R, Bilan HK, Gale JD, Wanni J, Madireddy G, Sealy MP, Achuthan A. Ultrasonic impact treatment (UIT) combined with powder bed fusion (PBF) process for precipitation hardened martensitic steels. *Additive Manufacturing.* 2024;84: 104078.
19. Fields B, Amiri M, Lim J, Purstl JT, Begley MR, Apelian D, Valdevit L. Microstructural control of a multi-phase PH steel printed with laser powder bed fusion. *Advanced Materials Technologies.* 2024;9: 2301037.
20. Kugelmeier CL, Unti LFK, Júnior ELS, Souza NM, Jardini AL, Avila JA, Cintho OM, Zilnyk K. Microstructure evolution and corrosion resistance evaluation of 17-4 precipitation hardening stainless steel processed by laser powder bed fusion. *Journal of Materials Engineering and Performance.* 2025;34: 10537–10547.
21. Wilson AW, Madison JD, Spanos G. Determining phase volume fraction in steels by electron backscattered diffraction. *Scripta Materialia.* 2001;45: 1335–1340.
22. Wu J, Wray PJ, Garcia CI, Hua M, De AJ. Ardo Image quality analysis: A new method of characterizing microstructures. *ISIJ International.* 2005;45: 254–262.
23. Nowell MM, Wright SI, Carpenter JO. Differentiating ferrite and martensite in steel microstructures using electron backscatter diffraction. In: *Proc. Materials Science and Technology Conference and Exhibition.* 2009.
24. Calcagnotto M, Ponge D, Raabe D. Microstructure control during fabrication of ultrafine grained dual-phase steel: Characterization and effect of intercritical annealing parameters. *ISIJ International.* 2012;52(5): 874–883.
25. Kang JY, Park SJ, Moon MB. Phase analysis on dual-phase steel using band slope of electron backscatter diffraction pattern. *Microscopy and Microanalysis.* 2013;19: 13–16.
26. Im YR, Kim EY, Song T, Lee JS, Suh DW. Tensile properties and stretch-flangeability of TRIP steels produced by quenching and partitioning (Q&P) process with different fractions of constituent phases. *ISIJ International.* 2021;61(2): 572–581.
27. Shen C, Wang C, Huang M, Xu N, Zwaag S, Xu W. A generic high-throughput microstructure classification and quantification method for regular SEM images of complex steel microstructures combining EBSD labeling and deep learning. *Journal of Materials Science & Technology.* 2021;93: 191–204.
28. Ostormujof TM, Purohit RRPPR, Breumier S, Gey N, Salib M, Germain L. Deep learning for automated phase segmentation in EBSD maps. A case study in dual phase steel microstructures. *Materials Characterization.* 2022;184: 111638.
29. Kang JY. Qualities of electron backscatter diffraction patterns and image contrast from a ferritic-martensitic steel microstructure. *Materials Characterization.* 2022;187: 111826.
30. Kozlowska A., Radwanski K., Grajcar A. Identification of structural constituents in advanced multiphase high-strength steels using electron back-scattered diffraction. *Symmetry.* 2024;16(12): 1630.
31. Stormvinter A, Mitsche S, Cerjak H. Martensite laths in creep resistant martensitic 9-12% Cr steels – calculation and measurement of misorientations. *Materials Characterization.* 2007;58(10): 874–882.
32. Govindaraj V, Farabi E, Kada S, Hodgson PD, Singh RP, Rohrer GS, Beladi H. Effect of manganese on the grain boundary network of lath martensite in precipitation hardenable stainless steels. *Journal of Alloys and Compounds.* 2021;886: 161333.
33. Kim JH, Miyamoto G, Shibata A, Hojo T, Koyama M, Zhang Y, Furuhara T. Influence of austenite grain boundary misorientation on hydrogen-induced intergranular crack propagation in a medium carbon martensitic steel. *Acta Materialia.* 2024;274: 120036.
34. Moura AN, Favarato LNO, Amorim DSC, Alcantara CM, Marques MCS, Orlando MTD, Vieira EA, Labiapari WS, Cunha MA, Oliveira TR. Effect of austenitization temperature on microstructure, crystallographic aspects, and mechanical properties of AISI 420 martensitic stainless steel. *Materials Science and Engineering: A.* 2024;909: 146835.
35. Sun Y, Wu Z, Ji Y, Wang P, Wu S, Cao G, Liu Z. Cryogenic impact toughness of 5.5 % Ni steel at −196 °C: synergy of a dual-phase heterogeneous lamellar structure and the stability of reversed austenite. *Materials Science and Engineering: A.* 2025;943: 148740.
36. Sun H, Shao M, Lu N, Li X, Li L, Wang Z, Jiang J, Zhang H. The morphology and crystallography of lath martensite via high pressure martensitic transformation in Fe-0.45 wt.% C steel. *Acta Materialia.* 2025;284: 120624.
37. Aletdinov AF, Mironov S, Korznikova GF, Zaripova RG, Konkova TN, Myshlyaev MM. EBSD analysys of austenite steel microstructure after cryogenic rolling. *Materials Physics and Mechanics.* 2017;33(1): 29–40. (In Russian)
38. Humphreys FJ. Quantitative metallography by electron backscatter diffraction. *Journal of Microscopy.* 1999;195: 170–185.